



Institut für Numerische Simulation

Rheinische Friedrich-Wilhelms-Universität Bonn

Wegelerstraße 6 • 53115 Bonn • Germany
phone +49 228 73-3427 • fax +49 228 73-7527
www.ins.uni-bonn.de

M. Griebel, M. Klitz

**Simulation of Droplet Impact with Dynamic
Contact Angle Boundary Conditions**

INS Preprint No. 1302

January 2013

Simulation of Droplet Impact with Dynamic Contact Angle Boundary Conditions

Michael Griebel and Margrit Klitz

Abstract The numerical simulation of dynamic wetting processes is of interest for a vast variety of industrial processes, where practical experiments are costly and time-consuming. In these simulations, the dynamic contact angle is a key parameter, but the modeling of its behavior is poorly understood so far. In this article, we simulate droplet impact on a dry flat surface by using two different contact angle models. Both models show good qualitative and quantitative agreement with experimental results. For our numerical method, we solve the three-dimensional Navier-Stokes equations with finite differences on a staggered grid. The free surface is captured by a level-set method, and the contact angle determines the shape of the level-set function at the boundary. Additionally, we investigate the mass-conservation properties of two volume-correction methods, which are invaluable for the analysis of the droplet behavior.

1 Introduction

The numerical simulation of dynamic wetting processes is of critical importance for a number of industrial applications such as coating, lamination, lubrication or ink- and spray-painting. All these applications have in common that liquid comes into contact with a solid surface and that the phase boundary is in motion. Thereby, a moving contact-line is produced along the substrate, which is the line where the air is replaced by the liquid. The quality of the wetting highly controls the quality of the industrial end products and, therefore, needs to be optimized to reduce wetting defects and instabilities such as air entrainment or ribbing. Here, numeri-

Michael Griebel
Institute for Numerical Simulation, Wegelerstr. 6, 53115 Bonn e-mail: griebel@ins.uni-bonn.de

Margrit Klitz
Institute for Numerical Simulation, Wegelerstr. 6, 53115 Bonn e-mail: klitz@ins.uni-bonn.de

cal simulation and optimization is a reliable and cheap alternative to the traditional time-consuming adjustment of machines and the expensive waste of raw materials.

Despite the industrial interest in the numerical simulation of dynamic wetting processes, the existing theoretical and numerical approaches so far often fail to correctly predict the results of practical experiments. This is due to two fundamental difficulties which constitute the so-called ‘moving-contact line problem’: First, the classical theory of continuum fluid mechanics (i.e. the Navier-Stokes equations with the no-slip condition for the velocity) predicts a shear stress singularity at the moving contact line. The second difficulty is the modeling of the contact angle which is usually required as a boundary condition and determines the shape of the free surface at the contact line.

Numerous mathematical models have been developed to remedy the moving contact-line problem. Most of them remove the stress-singularity, but are unable to describe the contact angle and flow behavior as observed in practical experiments; see [15] and the references therein. One of the few models, which considers the overall physical context of the moving contact line problem, is Shikhmurzaev’s interface formation model [15]. This model not only removes the stress-singularity, but is also able to describe a large variety of flows with singularities such as break-up, coalescence or cusp formation.

In this article we couple a reduced version of Shikhmurzaev’s interface formation model with our three-dimensional incompressible two-phase Navier-Stokes solver. For this solver, we employ a standard discretization on uniform Cartesian staggered grids and use Chorin’s projection approach. The free surface between the two fluid phases is tracked with the level-set approach. Here, the interface conditions are implicitly incorporated into the momentum equations by the continuum surface force (CSF) [2] method. Surface tension is evaluated using a smoothed delta function and third order interpolation. The parallelization of the code is based on conventional domain decomposition techniques using MPI. This allows us to deal with reasonably fine mesh resolutions in three dimensions.

For the simulation of dynamic wetting problems, our numerical scheme has to be mass conservative. Otherwise, the comparison of, e.g., numerically evaluated droplet diameters with those from experiments is impossible. However, the conventional level-set approach is rather renowned for its lack of mass conservation. Therefore, we investigate two different techniques for a better conservation of mass in this article [4, 20].

A further difficulty stems from the need for a correct implementation of the contact angle, which is necessary as a boundary condition for the level-set function ϕ for the computation of curvature, the level-set advection step and the reinitialization equation. Here, we present a new Neumann boundary condition for the level-set function, which is a refined version of the approach used in [9, 13].

The contribution of this article is as follows: We present a simple and effective way to include dynamic contact angle models into three-dimensional flow solvers. Furthermore, we extend the droplet impact study by Yokoi et al. [23] to three dimensions and compare their contact angle model to the reduced interface formation

model by Shikhmurzaev [15]. Thereby, we obtain droplet shapes and diameters, which compare well with those from practical experiments.

The remainder of this article is organized as follows: The first section is dedicated to the details of the moving contact line problem, i.e. to the difficulties involved in the modeling of the dynamic contact angle and to its numerical implementation. In the second section, we discuss our Navier-Stokes solver and the implemented level-set method. We then explain how the contact angle can be included as a boundary condition for the level-set function. Additionally, the dynamic contact angle has to be modeled: Here, we present the model by Yokoi et al. and the interface formation model by Shikhmurzaev. In the third section, we describe the discretization of our two-phase Navier-Stokes solver. We discuss the discretization of the contact angle boundary condition and the incorporation of the dynamic contact angle models into our flow solver. Moreover, we present two different methods to improve on the mass conservation properties of our approach. In the fourth section, we simulate droplet impact behavior on a dry surface and compare the evolving droplet shapes and diameters to those obtained from practical experiments. Furthermore, we compare our two improved mass conservation methods and discuss their convergence behavior. Finally, we give some concluding remarks.

2 The Moving Contact Line Problem

In this section, we describe the moving contact line problem and some of the current mathematical models for its solution. In this discussion, we include the two contact angle models by Yokoi et al. [23] and Shikhmurzaev [15], which we use in this article. Furthermore, tackling the problem from a numerical point of view, we address the question how the dynamic contact angle can be incorporated into our two-phase Navier-Stokes solver.

2.1 Modeling Issues

The key to the solution of the moving contact line problem is twofold: On the one hand, the stress singularity has to be removed and, on the other hand, the contact-angle behavior has to be modeled accurately.

In the framework of the so-called ‘slip models’ both problems are addressed independently: First, the no-slip condition for the velocity is relaxed and the fluid is allowed to slip at the contact line (see, e.g., [7, 8, 17]), which eliminates the stress singularity. Then, the contact angle θ_d is often chosen as a function

$$\theta_d = f(\text{Ca}, \theta_s, k_1, k_2, \dots). \quad (1)$$

of the contact line speed with the capillary number Ca , the static contact angle θ_s and material-related parameters k_i , which are used to fit the numerical results to the experiments.

A fundamental difficulty with these models is, for example, that they fail to describe the dependency of the contact angle on the flow rate, which is however, observed in experiments [15]. Thus, the dynamic contact angle is not simply a function of the contact-line speed and the material properties of the contacting media as assumed in equation (1). Instead, even for the same contact line speed, the dynamic contact angle can be changed by e.g. changing the flow field or geometry near the contact line. For example, in the curtain coating context, Blake et al. [1] have shown that for a fixed substrate speed, the observed contact angle varies with the flow rate and curtain height. This effect has been termed the ‘hydrodynamic assist of wetting’ and it cannot be described by an equation such as (1) – where the contact angle depends foremost on the speed of the contact line.

In the theory of thin films, the moving contact line problem is circumvented by assuming that the surface is already covered by a thin film of fluid [22]. Then, with a scaled lubrication approximation, one can derive Tanner’s law

$$U = A\theta^3, \quad (2)$$

where θ is now an apparent contact angle, which can be defined anywhere on the free surface. Here, U is a dimensionful velocity and A depends on the fluid properties. This law is often used for the modeling of the contact angle behavior in the framework of slip models as a variant of equation (1) and becomes

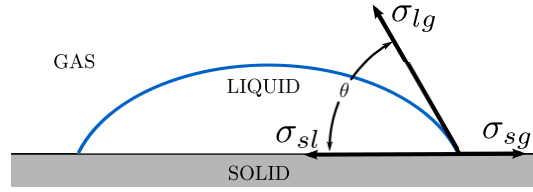
$$Ca = k(\theta_d - \theta_s)^3. \quad (3)$$

This use of Tanner’s law is conceptually questionable [15, p. 165], since there is no actual contact angle involved in the derivation of Tanner’s law in the first place. In this article, we use a related kind of slip model which has been improved and extended by Yokoi et al. [23].

Instead of an ad-hoc and separable treatment of the moving contact-line problem, Shikhmurzaev [15] considers its overall physical context in the derivation of his model for the formation and disappearance of interfaces. Let us shortly state his idea: We know from experimental observation that the dynamic contact angle differs from the static one and that the Young equation (Fig. 1) holds. Therefore, we can conclude that the surface tensions in the Young equation become dynamic as well, when the phase boundary is in motion. The fluid particles at the different interfaces relax to their new equilibrium values. This process occurs in finite time and is captured by Shikhmurzaev’s interface formation model.

In contrast to other approaches, the interface formation model not only removes the singularity, but is able to predict the experimentally observed rolling motion of the interface, as well as the dependence of the contact angle on the flow field. Within the literature, Shikhmurzaev’s interface formation model has been considered scarcely so far, which is mostly due to its complexity (see [15] and the references therein and [19]). Therefore, we consider a reduced version of the interface

Fig. 1 Young's force diagram: $\sigma_{sg} = \sigma_{sl} + \sigma_{lg} \cos \theta$. Here, σ_{sg} is the solid/gas, σ_{sl} the solid/liquid and σ_{lg} the liquid/gas interfacial tension.



formation model for small capillary numbers in this article. However, even this simplified model has been scarcely used so far [5, 11, 16].

Obviously, there are fundamental differences between both contact angle models considered in this article: The contact angle model by Yokoi et al. lacks a thorough underlying mathematical theory. It is developed for and based on a single droplet impact experiment only. A straightforward application of this model to the numerical simulation of other wetting experiments is difficult. Rather, this model is a prescription of contact angle values which fit well with a specific practical experiment. Since the prescribed dynamic contact angle values are very close to the ones observed in the experiment, the modeling error for the specific experiment is very small. Therefore, it gives us the opportunity to test our contact angle implementation as well as our methods for volume conservation and compare them to the results of the experiments.

On the other hand, behind Shikhmurzaev's model, there is a whole theoretical framework to explain the formation and disappearance of interfaces. This model is able to describe a vast variety of dynamic wetting phenomena. However, we use the reduced interface formation model, which is derived for small capillary numbers only. Therefore, we expect to obtain an approximate and smoothed contact line speed-contact angle relationship compared to the practical experiments and Yokoi's results in [23]. Still, the reduced model is an excellent trade-off between the complex full interface formation model and an easily implementable and reasonably accurate dynamic contact angle model. This will be seen in the remainder of this article.

2.2 Numerical Issues

Numerically, we have to address the difficulty of the correct implementation of the contact angle, which is needed as a boundary condition for the level-set function ϕ .

In the literature, a number of different approaches for the contact angle boundary condition of the level-set function can be found: Here, the simplest model is the zero Neumann boundary condition, which effectively fixes the contact angle to be 90° . If θ is variable, the implementation is less clear. One of the main approaches [23, 24] was developed by Sussman [21]. Here, the contact angle is taken into account by extrapolating the liquid interface, represented by the level-set function, into the solid. This approach requires the construction of an appropriate extension velocity, but the exact location of the position of the contact-line is not needed. Moreover,

in a method by Spelt [18], contact-line position and contact angle or contact line velocity are determined iteratively.

In [25] the movement of the contact line is induced by diffusion. Instead of using a direct relation between the gradient of the level-set function and the normal of the interface, a regularized normal vector field is constructed to avoid flux of ϕ over the boundary. Thereby, two additional regularization parameters appear, which influence the shape of the free surface at the contact line.

In [9, 13] a Neumann boundary condition for the level-set function is derived as follows: Let our fluid flow domain Ω be a box and $\mathbf{x} = (x, y, z) \in \Omega$. Then, at e.g. the wall $y = 0$, the geometric relation

$$\mathbf{n}_l \cdot \mathbf{n}_w = \cos \theta \quad (4)$$

holds for the contact angle θ . Here, \mathbf{n}_l is the outward surface normal and $\mathbf{n}_w = (0, -1, 0)^t$ is the outward normal at $y = 0$. Now, a Neumann boundary condition for the level-set function can be prescribed by rewriting relation (4) as

$$\phi_y = -\cos \theta \text{ for } \|\phi\| = 1. \quad (5)$$

However, the condition $\|\phi\| = 1$ is not always fulfilled. Thus, the recovery of this property of the level-set function is achieved by some reinitialization equation in the first place. In this article, we extend this approach and show that

$$\phi_y = -\cot \theta \sqrt{\phi_x^2 + \phi_z^2} \text{ for } 0 < \theta < \pi \quad (6)$$

without further assumptions on ϕ . Similar techniques have already been used by Fang et al. [6] and Mourik [12] within the volume-of-fluid approach. Note here, that our approach is consistent with the extension technique by Sussman [21] for the case that the geometry is a box. Like in his approach, we do not need to locate the exact contact line position. Additionally, relation (6) allows us to set contact angle boundary conditions for complex geometrical objects in our fluid flow domain¹.

3 Mathematical Model

In this section, we discuss the mathematical model for the three-dimensional flow of two immiscible incompressible fluids. We show how the contact angle can become a boundary condition for the level-set function and present two different models for the dynamic contact angle as given by Yokoi et al. [23] and Shikhmurzaev [15].

¹ Then, contact angles at corner cells of the geometry have to fulfill further restrictions as described in [6].

3.1 The Navier-Stokes solver

The behavior of the fluids is governed by the incompressible Navier–Stokes equations defined on an open set $\Omega = \Omega_1 \cup \Omega_2 \cup \Gamma_f \subset \mathbb{R}^3$ with Lipschitz boundary $\Gamma := \partial\Omega$. The two fluid domains Ω_1 and Ω_2 and the free interface $\Gamma_f := \partial\Omega_1 \cap \partial\Omega_2$ depend on time. We capture the interface by a level-set formulation, and surface tension effects are included via the CSF method [2]. Thus,

$$\begin{aligned} \rho(\phi)(\partial_t \mathbf{u} + (\mathbf{u} \cdot \nabla) \mathbf{u}) + \nabla p &= \nabla \cdot (\mu(\phi) \mathbf{S}) - \sigma \kappa(\phi) \delta(\phi) \nabla \phi + \rho(\phi) \mathbf{g} \\ \nabla \cdot \mathbf{u} &= 0 \end{aligned} \quad (7)$$

with time $t \in [0, T]$, fluid velocity \mathbf{u} , pressure p and volume forces \mathbf{g} . Here, μ is the viscosity and ρ the density. The fluid stress tensor is defined by $\mathbf{S} = \nabla \mathbf{u} + (\nabla \mathbf{u})^t$. The curvature of the free surface is given by κ , the surface tension is denoted by σ , and δ is the one-dimensional Dirac-delta functional introduced in the CSF approach.

We choose a level-set function ϕ as a signed-distance function such that

$$\phi(\mathbf{x}, t) \begin{cases} < 0 & \text{if } \mathbf{x} \in \Omega_1 \\ = 0 & \text{if } \mathbf{x} \in \Gamma_f \\ > 0 & \text{if } \mathbf{x} \in \Omega_2 \end{cases} \quad (8)$$

holds and the Eikonal equation $\|\nabla \phi\| = 1$ is fulfilled. The interface between the two fluids is then given by the zero level-set of ϕ :

$$\Gamma_f(t) = \{\mathbf{x} : \phi(\mathbf{x}, t) = 0\} \quad (9)$$

for all times $t \in [0, T]$. The level-set function is advected by the pure transport equation

$$\phi_t + \mathbf{u} \cdot \nabla \phi = 0 \quad (10)$$

with initial value $\phi_0(\mathbf{x}) = \phi(\mathbf{x}, 0)$.

With the help of ϕ we define the density ρ and the viscosity μ on the whole domain, i.e., on both fluid-phases. To this end, we set

$$\rho(\phi) := \rho_2 + (\rho_1 - \rho_2)H(\phi) \quad \text{and} \quad \mu(\phi) := \mu_2 + (\mu_1 - \mu_2)H(\phi), \quad (11)$$

where $H(\phi)$ denotes the Heaviside function which is defined as

$$H(\phi) := \begin{cases} 0 & \text{if } \phi < 0 \\ \frac{1}{2} & \text{if } \phi = 0 \\ 1 & \text{if } \phi > 0. \end{cases} \quad (12)$$

The Navier-Stokes equations (7) have to be complemented with boundary conditions for the pressure, the velocity and the level-set function.

In the next subsection, we present a boundary condition for the level-set function, which is required for the transport equation (10), the level-set reinitialization and the computation of the curvature κ . This condition determines the shape of the free

surface at the contact line and, therefore, depends on the dynamic contact angle θ_d as soon as the contact line is moving.

Finally, in addition to the standard equations of fluid dynamics described above, the dynamic contact angle has to be modeled properly, which will be presented in Subsections 3.3 and 3.4.

3.2 The Contact Angle as a Boundary Condition

As already exemplified in Subsection 2.2, we now formulate a Neumann boundary condition for the level-set function, which incorporates the dynamic contact angle. Thus, at the boundary of Ω the contact angle is defined by the geometric relation

$$\mathbf{n}_l \cdot \mathbf{n}_w = \cos(\theta), \quad (13)$$

where θ is the contact angle (static or dynamic), \mathbf{n}_w is the outward normal drawn from the flow region into the boundary, and \mathbf{n}_l is normal to the level-set function which points from the fluid phase with lower level-set values to the one with higher values, i.e.

$$\mathbf{n}_l = \frac{\nabla\phi}{\|\nabla\phi\|}. \quad (14)$$

Then, the boundary condition for the level-set function is given in the following proposition.

Proposition 1. *At any wall of Ω , whose outward normal is given by $\mathbf{n}_w^i = \pm \mathbf{e}^i$ for some $i \in \{1, 2, 3\}$, the level-set's i -th derivative ϕ_{x_i} can be related to θ by*

$$\phi_{x_i} = \pm \cot(\theta) \sqrt{\sum_{j=1, j \neq i}^3 \phi_{x_j}^2} \quad (15)$$

for any angle $0 < \theta < \pi$.

Proof. We prove this proposition here for two walls with outward normals $\mathbf{n}_w^2 = -\mathbf{e}^2$ and $\mathbf{n}_w^3 = \mathbf{e}^3$, since the cases $\mathbf{n}_w^i = \pm \mathbf{e}^i$ for $i = 1$ or $i = 3$ can be treated in the very same way. For both boundaries, we have to distinguish between the cases $0 < \theta \leq \frac{\pi}{2}$ and $\frac{\pi}{2} < \theta < \pi$.

Let $\mathbf{n}_w^2 = -\mathbf{e}^2 = (0, -1, 0)^t$. Then, from equation (13) and (14), we have

$$\mathbf{n}_l \cdot \mathbf{n}_w^2 = \cos(\theta) \Leftrightarrow -\phi_{x_2} = \cos(\theta) \|\nabla\phi\|. \quad (16)$$

First, let $0 < \theta \leq \frac{\pi}{2}$. Then, $0 \leq \cos(\theta) < 1$ and $\sin^2(\theta) = 1 - \cos^2(\theta) > 0$. Since $\cos(\theta) \geq 0$, we conclude that $-\phi_{x_2} \geq 0$ as well, and define the positive function $\tilde{\phi} := -\phi_{x_2}$ with $\tilde{\phi}^2 = \phi_{x_2}^2$. Inserting $\tilde{\phi}$ into equation (16), we obtain

$$\tilde{\phi} = \cos(\theta) \sqrt{\phi_{x_1}^2 + \tilde{\phi}^2 + \phi_{x_3}^2}.$$

Now, only positive variables constitute both sides of the equation. Thus, we are allowed to take the square of both sides and still obtain the equivalent relation

$$\begin{aligned}
\tilde{\phi}^2 &= \cos^2(\theta)(\phi_{x_1}^2 + \tilde{\phi}^2 + \phi_{x_3}^2) \\
\Leftrightarrow \tilde{\phi}^2(1 - \cos^2(\theta)) &= \cos^2(\theta)(\phi_{x_1}^2 + \phi_{x_3}^2) \\
\Leftrightarrow \tilde{\phi}^2 &= \frac{\cos^2(\theta)}{\sin^2(\theta)}(\phi_{x_1}^2 + \phi_{x_3}^2) \\
\Leftrightarrow \tilde{\phi} &= \frac{\cos(\theta)}{\sin(\theta)}\sqrt{\phi_{x_1}^2 + \phi_{x_3}^2}.
\end{aligned}$$

Again, taking the root to obtain the last equivalency relation is only allowed since all parts of the equation (including $\sin^2(\theta)$) are greater than or equal to zero. Then, for $0 < \theta \leq \frac{\pi}{2}$, we have $\sin(\theta) = \sqrt{1 - \cos^2\theta}$. Resubstituting $\tilde{\phi} = -\phi_{x_2}$, we obtain the desired result

$$\phi_{x_2} = -\cot(\theta)\sqrt{\phi_{x_1}^2 + \phi_{x_3}^2}.$$

Now, let $\frac{\pi}{2} < \theta < \pi$. Then, $-1 < \cos\theta < 0$ and $\sin^2(\theta) = 1 - \cos^2(\theta) > 0$. From equation (16), we know that $\phi_{x_2} > 0$, since $\cos\theta < 0$. We define the positive function $\tilde{c} := -\cos(\theta)$ with $\tilde{c}^2 = \cos^2(\theta)$ and obtain likewise

$$\phi_{x_2} = \tilde{c}\sqrt{\phi_{x_1}^2 + \phi_{x_2}^2 + \phi_{x_3}^2} \Leftrightarrow \phi_{x_2} = -\cot(\theta)\sqrt{\phi_{x_1}^2 + \phi_{x_3}^2}.$$

In the second part of this proof, the outward normal of the boundary is given by $\mathbf{n}_w^2 = \mathbf{e}^2$. Then, from equation (13) and (14), we have

$$\mathbf{n}_l \cdot \mathbf{n}_w^2 = \cos(\theta) \Leftrightarrow \phi_{x_2} = \cos(\theta)\|\nabla\phi\|. \quad (17)$$

Again, we consider the two cases $0 < \theta \leq \frac{\pi}{2}$ and $\frac{\pi}{2} < \theta < \pi$. First, let $0 < \theta \leq \frac{\pi}{2}$. Then, $0 \leq \cos\theta < 1$ and $\sin^2(\theta) = 1 - \cos^2(\theta) > 0$. From equation (17), we know that $\phi_{x_2} > 0$, since $\cos\theta > 0$. Similar to the first case above, we can then show that

$$\phi_{x_2} = \cos(\theta)\sqrt{\phi_{x_1}^2 + \phi_{x_2}^2 + \phi_{x_3}^2} \Leftrightarrow \phi_{x_2} = \cot(\theta)\sqrt{\phi_{x_1}^2 + \phi_{x_3}^2}.$$

Now, let $\frac{\pi}{2} < \theta < \pi$. Then, $-1 < \cos\theta < 0$ and $\sin^2(\theta) = 1 - \cos^2(\theta) > 0$. From equation (17), we know that $-\phi_{x_2} > 0$, since $\cos\theta < 0$. We define the positive function $\tilde{c} := -\cos(\theta)$ with $\tilde{c}^2 = \cos^2(\theta)$ and the positive function $\tilde{\phi} := -\phi_{x_2}$ with $\tilde{\phi}^2 = \phi_{x_2}^2$. With these definitions and similar equivalency relations as in all the other cases, we obtain

$$\tilde{\phi} = \tilde{c}\sqrt{\phi_{x_1}^2 + \tilde{\phi}^2 + \phi_{x_3}^2} \Leftrightarrow \phi_{x_2} = \cot(\theta)\sqrt{\phi_{x_1}^2 + \phi_{x_3}^2}.$$

□

The above proposition allows us to write the contact angle θ as a boundary condition of the level-set function. Now, the hard part is a reliable model for the dynamic contact angle $\theta = \theta_d$. In the next two subsections, we will describe two different dynamic contact angle models, which we will later employ in our numerical method.

3.3 The Dynamic Contact Angle Model by Yokoi et al. (C1)

Yokoi et al. [23] propose a dynamic contact angle model, which combines Tanner's law (3) with a static advancing and receding contact angle, since Tanner's law holds for small capillary numbers only. In the combined model, similar to what is observed in experiments, the contact angle tends to both the limit of a maximum advancing angle θ_{mda} as the dimensionful contact line speed u_{cl} increases and the limit of a minimum dynamic receding angle θ_{mdr} as u_{cl} decreases:

$$\theta_d = \begin{cases} \min\{\theta_s + \left(\frac{\mu u_{\text{cl}}}{\sigma k_a}\right)^{\frac{1}{3}}, \theta_{\text{mda}}\} & \text{if } u_{\text{cl}} \geq 0 \\ \max\{\theta_s + \left(\frac{\mu u_{\text{cl}}}{\sigma k_r}\right)^{\frac{1}{3}}, \theta_{\text{mdr}}\} & \text{if } u_{\text{cl}} < 0. \end{cases} \quad (\text{C1})$$

Here, θ_s is the static contact angle, and the material-related parameters k_a and k_r are adjusted to fit the numerical results to the results obtained measurements. Furthermore, the stress singularity is circumvented by inducing numerical slip for the velocity at the contact line.

3.4 The Dynamic Contact Angle Model by Shikhmurzaev (C2)

The second model for the dynamic contact angle at small capillary number is a reduced version of Shikhmurzaev's interface formation model [15]. The full model accounts for different classes of flows, where interfaces are formed or destroyed. The equations, which capture the surface tension relaxation process and have to be solved on the surface itself, are derived from mass, momentum and energy conservation. For the case of small capillary and Reynolds numbers, we can analyze them as a local problem whose solution can be incorporated into various types of global flow problems. Here, lots of experimental works simplify the verification of numerical results.

We follow the description in [15]. There, the flow domain is split into two asymptotic regions, and in both the limit $\text{Ca} \rightarrow 0$ is studied analytically. In the inner asymptotic region to leading order in Ca the dynamic contact angle and the dimensionless contact-line speed V are related by

$$\cos(\theta_s) - \cos(\theta_d) = \frac{2V [\cos(\theta_s) - \sigma_{sg} + (1 - \rho_G^s)^{-1} (1 + \rho_G^s u_{(12)}(\theta_d, k_\mu))]}{V + [V^2 + 1 + (\cos(\theta_s) - \sigma_{sg})(1 - \rho_G^s)]^{\frac{1}{2}}} \quad (C2)$$

with θ_s the static contact angle, k_μ the gas-to-liquid viscosity ratio, and $\rho_G^s \equiv 1 - \frac{\sigma_{sg} - \sigma_{sl}}{\lambda \cos \theta_d}$, where σ_{sg} and σ_{sl} denote the surface tension in the gas-solid and liquid-solid interface, respectively, and λ is a material parameter. Here, the radial velocity $u_{(12)}(\theta_d, k_\mu)$ must be derived from the solution in the outer region.

In particular, in the outer region to leading order in Ca the free-surface curvature becomes zero and one obtains a flow problem in a wedge [15]. The solution to this problem was given by Moffatt in [10] as

$$u_{(12)}(\theta_d, 0) = \frac{\sin \theta_d - \theta_d \cos \theta_d}{\sin \theta_d \cos \theta_d - \theta_d}. \quad (18)$$

If the viscosity of the gas phase is taken into account, Moffatt's solution becomes

$$u_{(12)}(\theta_d, k_\mu) = \frac{(\sin \theta_d - \theta_d \cos \theta_d)K(\theta_2) - k_\mu(\sin \theta_2 - \theta_2 \cos \theta_2)K(\theta_d)}{(\sin \theta_d \cos \theta_d - \theta_d)K(\theta_2) + k_\mu(\sin \theta_2 \cos \theta_2 - \theta_2)K(\theta_d)}, \quad (19)$$

with $\theta_2 = \pi - \theta_d$ and $K(\theta) = \theta^2 - \sin^2 \theta$ [15].

Alternatively, $u_{(12)}(\theta_d, k_\mu)$ in (C2) can be replaced by the inner limit of the outer solution, i.e. by a numerically computed far field velocity sufficiently close to the contact line. This alters the dynamic contact angle for the same contact line speed and is exactly what is observed in laboratory experiments as the nonlocal influence of the flow field/geometry on the dynamic contact angle.

As described in [15], we introduce the reference velocity U and the scaling factor Sc by

$$U = \sqrt{\frac{\gamma \rho_0^s (1 + 4\alpha\beta)}{\tau\beta}} \quad \text{and} \quad \text{Sc} = \sqrt{\frac{\sigma^2 \tau\beta}{\mu^2 \gamma \rho_0^s (1 + 4\alpha\beta)}}. \quad (20)$$

Here, σ is the equilibrium surface tension, α and β are phenomenological constants depending on the 'state of the interface', γ is a phenomenological constant describing the compressibility of the fluid, τ is the surface tension relaxation time and ρ_0^s is the surface density for zero surface tension, both of which can be treated as material constants. Thus, Sc depends on the material properties of the fluid and the interface. Then, the dimensionless contact line velocity is given by

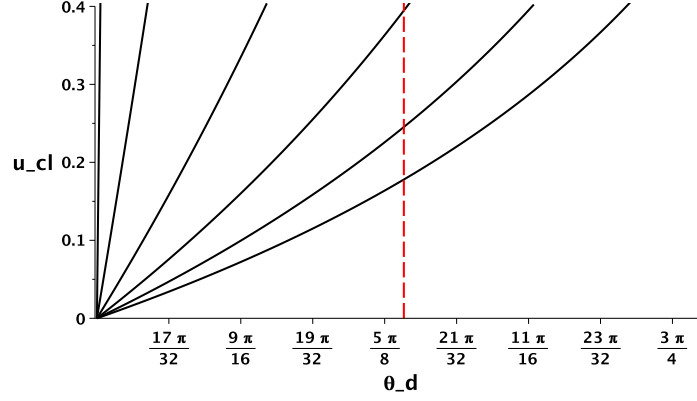
$$V = \frac{u_{cl}}{U} = \frac{u_{cl}\mu}{\sigma} \text{Sc}, \quad (21)$$

and Sc can be chosen to fit the numerical results to the experimental data.

Let us demonstrate how the dimensionless parameter Sc influences the results of equation (C2). As an example, we consider a droplet of distilled water which impacts on a silicon wafer onto which hydrophobic silane has been grafted. The equilibrium contact angle of the substrate with distilled water is 90° , and the relevant physical and numerical parameters of this experiment are listed in Table 1. Thus,

Table 1 Parameters for distilled water impacting on a silicon wafer onto which hydrophobic silane has been grafted.

distilled water: $\mu_l = 1.0_{-3} \text{ kg/ms}$, $\rho_l = 1_{\text{3}} \text{ kg/m}^3$	surface tension: $\sigma = 7.2_{-2} \text{ N/m}$
air: $\mu_g = 1.82_{-5} \text{ kg/ms}$, $\rho_g = 1.25_0 \text{ kg/m}^3$	surface thickness: $\varepsilon = 1.9h$
forces: $\mathbf{g} = (0, -9.81, 0) \text{ m/s}^2$	boundary conditions: no-slip
initial velocity: $\mathbf{u} = (0, -1.0, 0) \text{ m/s}$	droplet diameter 2.28_{-3} m
$\theta_{\text{mda}}: 114^\circ$	$k_a: 9.0_{-9}$
$\theta_{\text{mdr}}: 52^\circ$	$k_r: 9.0_{-8}$

**Fig. 2** Dynamic contact angle vs. dimensionful contact-line speed for different values of Sc given in [rad] and [m/s], respectively. From left to right: $Sc = 0.1, 1.5, 5.5, 11.5, 18.5, 25.5$. The straight dashed line corresponds to the maximum of the dynamic advancing contact angle of 114° observed in the experiments.

equation (C2) can be resolved with respect to positive V as given in [15]. Since we are interested in the relationship between the dynamic contact angle and the dimensionful contact line velocity, we also use equation (21) to plot the dimensionful speed-angle relationship for different values of Sc . The remaining parameters are chosen according to Table 1, $\rho_G^s = 0.9$, $\sigma_{sg} = 0$, and $u_{(12)}(\theta_d, 0)$ is determined by Moffatt's solution (18). The effect of the variation of Sc is shown in Figure 2: We see that the contact angle as a function of u_{cl} increases from its static value θ_s and tends the faster to 180° the more we increase Sc . The horizontal straight red line indicates the maximum dynamic advancing contact angle of 114° determined from the experiments. For $Sc = 11.5$ this value is reached at a maximum contact line speed of about $u_{cl} = 0.4 \text{ m/s}$.

4 The Numerical Method

In this section, we describe the discretization of the Navier-Stokes equations (7) in space and time with special emphasis on the level-set method. We discuss the implementation of the contact angle boundary condition and of the two contact angle models. Last, we present two methods for a better conservation of mass within the level-set method.

4.1 Discretization of the Navier-Stokes equations and the Level-Set Method

We discretize the Navier-Stokes equations with finite differences on a staggered uniform grid and use an explicit second-order Adams-Bashforth time integration scheme. The solution process is based on the well-known projection method: First, an intermediate velocity field \mathbf{u}^* , which may not be divergence free, is advanced by the Adams-Bashforth time scheme; second, we compute a correction ∇p^{n+1} of the intermediate velocity field by the pressure Poisson equation which leads to a divergence free velocity field \mathbf{u}^{n+1} . Thus, we treat the pressure implicitly and solve the Poisson equation by a Jacobi-preconditioned conjugate gradient method. A fifth-order weighted essentially non-oscillatory (WENO) scheme is used for the discretization of the convective transport of the Navier-Stokes equations (7) as well as for the level-set transport (10). The diffusion term is computed by using second-order central differences.

For the treatment of the free surface between the two fluid phases we employ the level-set approach [3, 4]. Here, the interface conditions are implicitly incorporated into the momentum equations by the continuum surface force (CSF) [2] method.

Note, that we have to reinitialize the level-set function ϕ^* after each transport step to recover its signed distance property $|\nabla \phi^{n+1}| = 1$ without disturbing the zero level-set. To generate the appropriate signed-distance function $\phi^{n+1}(\mathbf{x})$ with the same zero level-set as $\phi^*(\mathbf{x})$, we solve the following pseudo-transient Hamilton–Jacobi problem to steady state

$$\phi_\tau^* = \text{sign}(\phi_0)(1 - |\nabla \phi^*|) \quad (22)$$

with initial value $\phi_0 = \phi^*(\mathbf{x})$. Again, we discretize this equation by a fifth order WENO scheme in space and employ a third-order Runge-Kutta for its time-integration.

For reasons of numerical stability, we employ a regularized signum function

$$S(\phi^*) = \frac{\phi^*}{\sqrt{(\phi^*)^2 + |\nabla \phi^*|^2 (\delta x^2)}}. \quad (23)$$

and a smoothed Heaviside and Dirac-delta functional in an ε -environment of the free surface. Then the Hamilton–Jacobi problem reads

$$\phi_\tau^* = S(\phi^*)(1 - |\nabla\phi^*|). \quad (24)$$

For further details on the implementation of our Navier-Stokes solver NaSt3DGPF and of the level-set method see [3] and [4].

4.2 Discretization of the contact angle boundary condition

The discretization of the contact angle boundary condition (15) is very similar to the discretization of the standard Neumann boundary condition for the level-set function. Again, we exemplify this at the wall $y = 0$, where equation (15) becomes

$$\phi_y = -\cot(\theta)\sqrt{\phi_x^2 + \phi_z^2}. \quad (25)$$

On the staggered grid (Fig. 3), the level-set values are discretized in the cell center. Then, with grid cells denoted by integers (i, j, k) ,

$$\frac{\phi_{i,j,k} - \phi_{i,j-1,k}}{\delta y_j} = -\cot(\theta)\sqrt{\phi_{x_{i,j,k}}^2 + \phi_{z_{i,j,k}}^2}, \quad (26)$$

where δy_j is the mesh width. The derivatives $\phi_{x_{i,j,k}}$ and $\phi_{z_{i,j,k}}$ can be discretized by central differences. This equation can be solved for the staggered grid's ghost cell value $\phi_{i,j-1,k}$, which gives the required boundary condition for ϕ .

The values for the contact angle θ are computed by the discretized dynamic contact angle models of Yokoi et al. (C1) or Shikhmurzaev (C2), which we will discuss subsequently.

4.3 Implementation of the Contact Angle Models

In this subsection, we describe how the contact angle models are incorporated into our two-phase Navier-Stokes solver. For this, both models require the computation

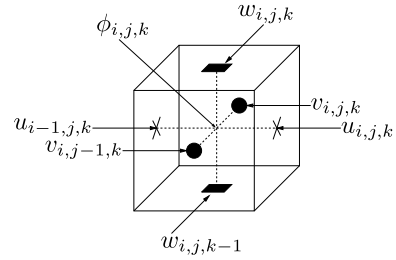


Fig. 3 On the staggered grid, the level-set function ϕ is discretized at the cell center and the velocity is discretized at the face centers of the grid.

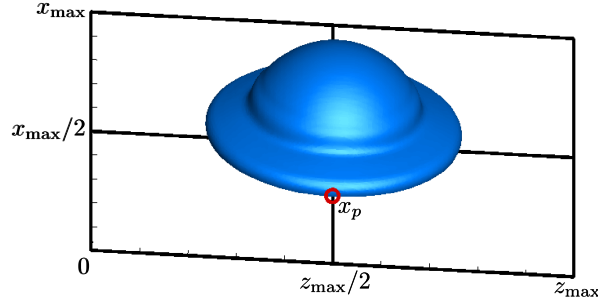


Fig. 4 The contact line velocity is evaluated at the contact point x_p at the intersection with the line $z = z_{\max}/2$.

of the contact line velocity u_{cl} . Additionally, for Shikhmurzaev's model, we also need the velocity $u_{(12)}(\theta_d, k_\mu)$.

In the following, we focus on the example of drop impact, and we assume that the drop spreads symmetrically (cf. Fig. 4). Then, u_{cl} is taken as the velocity value u in x -direction which is closest to the contact point x_p at the line $z_{\max}/2$ and still lies in the droplet's fluid phase. This simplified computation of the contact line velocity is also done by Yokoi et al. [23] and we stick to it for the sake of comparison.

Furthermore, we compute $u_{(12)}$ either by Moffatt's solution (18) or we use a velocity value of the far field. This far field velocity value is arbitrarily chosen to be about two grid cells away from the contact line. Thus, if e.g. at $y = 0$, $\phi_{i,1,k} \cdot \phi_{i+1,1,k} < 0$ and $\phi_{i,1,k}$ in the liquid phase, $u_{(12)} = u_{i-1,2,k}$. In the following, we will refer to these two options for $u_{(12)}$ as (M1) and (M2), respectively.

For (M1), the contact angle equation (C2) becomes nonlinear and we invoke a Newton iteration method to solve for θ_d . For (M2), the equation can be solved directly by evaluating the arccos-function. Here, if the argument of the arccos is not in $[-1, 1]$, we use Moffatt's solution (M1) instead.

All in all, the contact line models fit into our flow solver as follows:

1. Let θ^n be given from the previous time-step.
2. Solve the level-set advection equation (10) with the boundary condition (15) and $\theta = \theta^n$.
3. C1: Use a velocity value near x_p^{n+1} for u_{cl}^{n+1} and compute θ^{n+1} from equation (C1)
 C2: Use a velocity value near x_p^{n+1} for u_{cl}^{n+1} . Compute the radial velocity $u_{(12)}$ by (M1) or (M2) and θ^{n+1} from equation (C2).
4. Solve the level-set reinitialization (24) with the boundary condition (15) and $\theta = \theta^{n+1}$.

Finally, note that we use the no-slip condition for the velocity for both contact angle models. On the staggered grid, as drawn in Figure 3, the no-slip condition is never fulfilled exactly, which introduces enough numerical slip to eliminate the stress singularity at the contact line.

4.4 Methods for Mass Conservation

An important issue – especially for level-set methods – is mass conservation. In the reinitialization step the current level-set function is replaced by a smoother, less distorted function which has the same zero level-set. However, this also introduces numerical diffusion to the solution which leads to difficulties with volume conservation. To this end, we used a global and a local volume correction method to remedy this problem.

For the global volume correction, already described and investigated in [4], we employ a Picard iteration after the reinitialization step:

$$\phi^{n+1} \leftarrow \phi^{n+1} + \omega(V(\phi^0) - V(\phi^{n+1})). \quad (27)$$

Here, $V_i(\phi^0)$ is the initial volume of Ω_2^0 and $V(\phi^{n+1}) := \int_{\Omega} H(\phi^{n+1}) d\mathbf{x}$ denotes the volume of Ω_2^{n+1} at time $t = n + 1$ after the reinitialization procedure. The relaxation parameter ω depends on the specific problem and is chosen to minimize the number of iterations in the relaxation process.

For the local volume correction, we follow [20] in improving the re-distancing algorithm of the level-set function by formulating a constraint which conserves the volume of the domain and prevents the straying of the level-set function from its initial position. We require that

$$\partial_t \int_{\Omega} H(\phi^*) = 0 \quad (28)$$

and modify the Hamilton-Jacobi problem by

$$\phi_{\tau}^* = \text{sign}(\phi_0)(1 - |\nabla\phi^*|) + \lambda f(\phi^*). \quad (29)$$

Then we determine the time-dependent function λ by

$$\partial_{\tau} \int_{\Omega} H(\phi^*) = \int_{\Omega} H'(\phi^*) \phi_{\tau}^* = \int_{\Omega} H'(\phi^*) (\text{sign}(\phi_0)(1 - |\nabla\phi^*|) + \lambda f(\phi^*)), \quad (30)$$

i.e.

$$\lambda = \frac{-\int_{\Omega} H'(\phi^*) \text{sign}(\phi_0)(1 - |\nabla\phi^*|)}{\int_{\Omega} H'(\phi^*) f(\phi^*)}. \quad (31)$$

The choice of

$$f(\phi^*) = H'(\phi^*) |\nabla\phi^*| \quad (32)$$

ensures that the correction takes place at the interface only.

The discretization of the local mass correction in two-dimensions is described in [20]. In three dimensions, the numerical integration of some function g over the domain

$$\Omega_{ijk} = \{(x, y, z) \in \Omega : x_{i-\frac{1}{2}} < x < x_{i+\frac{1}{2}}, y_{j-\frac{1}{2}} < y < y_{j+\frac{1}{2}}, z_{k-\frac{1}{2}} < z < z_{k+\frac{1}{2}}\},$$

changes to

$$\int_{\Omega_{ijk}} g_{ijk} \, d\mathbf{x} \approx \frac{1}{78} \left[52g_{ijk}(\delta x_i \delta y_j \delta z_k) + \sum_{\substack{p,q,r=-1 \\ (p,q,r) \neq (0,0,0)}}^1 (g_{i+p,j+q,k+r}(\delta x_i \delta y_j \delta z_k)) \right].$$

Furthermore, in the original article [20], a non-smooth signum-function is employed. For better conservation properties and numerical stability, we again choose a smooth variant and replace $\text{sign}(\phi_0)$ by $S(\phi^*)$ as given in equation (24).

This volume correction is ‘local’ since the mass should remain unchanged in any sub-domain of Ω , so that $\int H(\phi^*)$ is preserved in every grid cell. It is also ‘local’ in a negative sense, since it only prevents the straying of the level-set function, but does not correct mass errors which occur due to the numerical diffusion introduced when solving the transport equation (10).

5 Numerical Results

In this section we evaluate the mathematical and numerical models for the example of a droplet impact simulation. Specifically, we consider a droplet of distilled water which impacts on a silicon wafer onto which hydrophobic silane has been grafted. The equilibrium contact angle of the substrate with distilled water is 90° , and the relevant physical and numerical parameters of this experiment have already been listed in Table 1.

The numerical simulation of this specific droplet impact scenario is valuable due to various reasons: First, Yokoi et al. [23] provide experimental results for the droplet behavior. Thus, we can compare the droplet shape, droplet diameter and dynamic contact angle from the physical experiments with the numerical results of our dynamic contact angle models (C1) and (C2). Additionally, we do not have to re-adapt the parameters k_a and k_r in (C1), since the contact angle model has been designed for this specific experiment. Second, Yokoi et al. [23] present two-dimensional numeric results in their work, which we can use for comparison with our three-dimensional results as well. Last, in this specific droplet impact experiment, the numerically computed droplet behavior is very sensitive to the applied contact angles: For example, using the static contact angle instead of a dynamic contact angle model causes the drop to rebound; the same happens if only static advancing and receding contact angles are applied; see [23] for further details. There-

fore, this specific kind of droplet impact simulation is a very sensitive test case for our Navier-Stokes solver, the implemented contact angle boundary condition and the two contact angle models.

However in the work of Yokoi et al., we also see the difficulty in obtaining accurate experimental results. There, the presented droplet shapes are obtained from a different experiment (E1) than the measured contact angle and diameter (E2). For the latter, only the right hand side of the droplet has been observed to increase the resolution around the contact line. If we compare the experimental droplet shapes in Figure 5 and 6 with the experimentally measured droplet diameter in Figure 7, we see that at times $t = 10$ and 15 ms the diameter of the droplet shapes (obtained from E1) is visibly smaller than the one given in Figure 7 (obtained from E2), which gives us an indication of the involved measuring error.

Let us give an example for the discrepancy between experiments (E1) and (E2). In Figures 5, 6 and 8 at $t = 4$ ms all numerical methods predict a horizontally wider droplet than the laboratory experiment (E1), which is depicted in the first row of the respective figures. However, if you compare this result with the diameter-time curve in Figures 7 and 9, the numerically computed droplet diameter at $t = 4$ ms reproduces the droplet diameter from the laboratory experiment (E2) nearly perfectly – at least for the highest numerical resolution, which is also used in the pictures for the droplet shapes.

In the following, we present our results in three steps: First, we take Yokoi’s model (C1) and compare the experimentally evaluated droplet shapes and diameters with our three-dimensional simulation computed by the pure level-set method and the two volume correction methods. Second, we use two variants of the reduced interface formation model (C2) to simulate the same droplet with global volume correction only. In a last step, we discuss the mass conservation behavior of our numerical methods.

5.1 The Contact Angle Model by Yokoi

In this subsection we present the results of the droplet impact simulation with the Navier-Stokes equations (7) and (C1). The numerically obtained droplet shapes (white) during the impact are shown in Figures 5 and 6 compared with experiments by [23] (black).

The results of the laboratory experiments (E1) are always shown in the first row of the respective figures. The second row corresponds to the computed numerical solution with the pure level-set method, i.e. without any volume-correction methods: We see that during the first three points in time (Fig. 5), when inertia is dominant, these droplet shapes compare very well with the experimental snapshots from (E1). At $t = 10$ ms the simulated droplet shape is still remarkably close to the experiment, while at the next time steps, the numerical droplet fails to reproduce the correct droplet height and width of the experiment (Fig. 6). This is partly due to its obvious loss in mass: Despite the very high resolution, the droplet still loses about 20% of

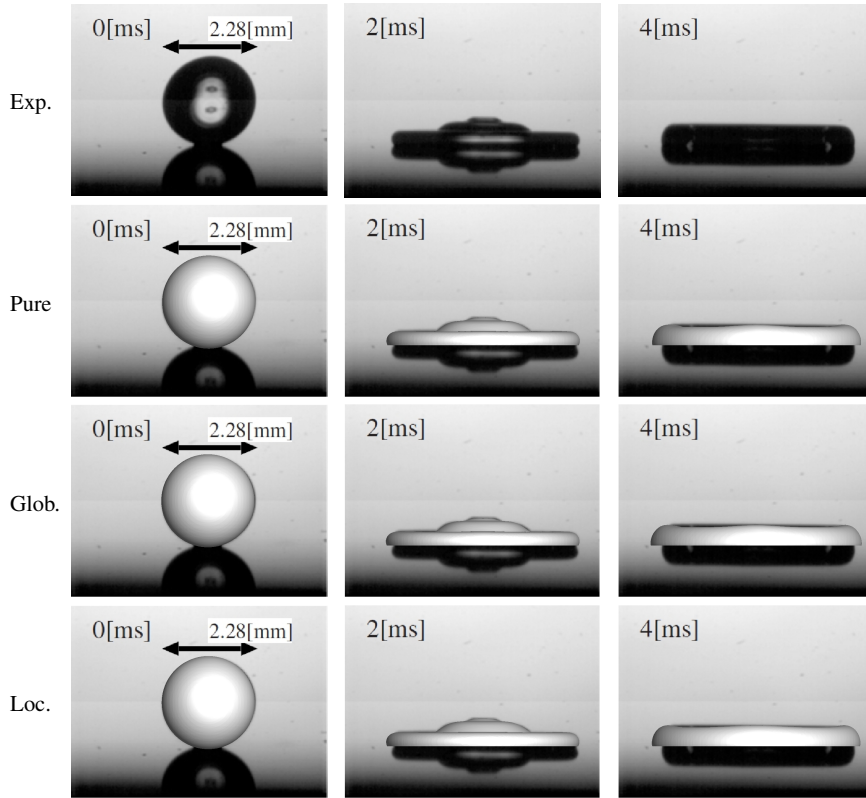


Fig. 5 Droplet impact $t = 0$ to 4 ms. In descending order: experimental results, pure level-set method, level-set with global volume-correction, level-set with local volume-correction.

its volume during the simulation. Thus, the comparison with the droplet diameter measured in the laboratory experiment (E2) becomes difficult as well. In Figure 7, we see that the pure level set method is unable to produce the final droplet diameter for all applied resolutions. Nevertheless, at about $t = 4$ ms the maximum diameter is well recovered and the overall behavior of the diameter-time curve is close to the experiment. We see here that the simulated droplet diameter at times $t = 10$ and 15 ms is closer to the experiment (E2) than to (E1). All in all, despite its obvious loss in volume and within the experimental measuring error, the pure level set method is able to produce simulation results, which correspond well with the experimentally observed droplet behavior.

At this point, we nevertheless see the need for volume-conserving simulation methods. Therefore, we simulate the droplet impact with the global volume correction and the local volume correction. The resulting droplet shapes are presented in the third and forth row of Figures 5 and 6.

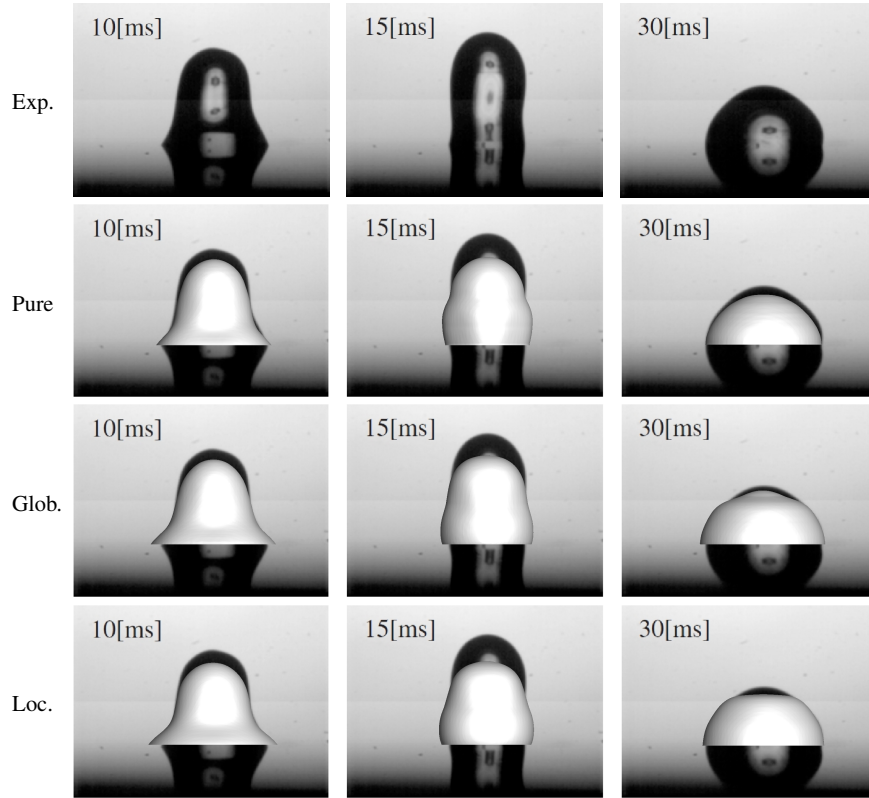


Fig. 6 Droplet impact $t = 10$ to 30 ms. In descending order: experimental results, pure level-set method, level-set with global volume-correction, level-set with local volume-correction.

We expect that the results from the global volume correction are very close to those by the pure level-set method, since the fix-point iteration tends to simply inflate the droplet. This is exactly what we observe in Figure 5 and 6: The droplet shapes recovered by the global correction method are similar to those by the pure level set method, but the volume of the drop is now preserved up to 100%. Again at the last three time steps, the droplet diameter produced by the global volume correction method is closer to experiment (E2) than to (E1). If we compare the droplet diameter with (E2), we see that its evolution over time is also very similar to the pure level-set method's results (Fig. 7). Due to the improved volume conservation, the maximum droplet diameter at $t = 4$ ms and the final droplet diameter are captured excellently by the global volume correction method.

Again, if we apply the local volume correction, we get results which compare better with (E2) than with (E1): The droplet diameter results agree well with the experimental ones, as we can see from Figure 7. For the first three points in time, the droplet shapes with the local volume correction method are in good agreement

with the other simulation results and the experiments (Fig. 5). However, we then get a slightly larger deviation from (E1) at times $t = 10$ and 15 ms (Fig. 6), where the droplet width is more overshoot than with the other two methods.

If we compare our two volume correction methods, we first note that both are able to conserve the volume of the droplet up to nearly 100% for the highest grid resolution. Second, we observe that the global volume correction simply inflates the droplet everywhere, while the local volume correction tends to widen the droplet horizontally. All in all, we conclude that both correction methods are in good agreement with the experimental results and lie well within the scope of the experimental error.

In a next step, we compare our three-dimensional results to the two-dimensional ones by Yokoi et al. obtained by a coupled level-set and volume-of-fluid method. The 2D droplet diameter is given in Figure 7 and is nearly indistinguishable from experiment (E2). Therefore, we must expect the computed 2D droplet shapes to deviate from (E1). These 2D droplet shapes can be found in Figure 8 of [23], where they are visualized as three-dimensional results. Contrary to our simulation, the droplet shape at $t = 2$ ms tends more to a pyramid shape and does not convincingly show the three layers obtained in the experiment. This might well be due to the lacking third dimension. Later, the two-dimensional results are comparable with our 3D results, but the width of the droplet at $t = 10$ ms is even larger than in our case. Here, we have to remember that the two parameters k_a and k_r in (C1) were used to fit Yokoi's 2D numerical results to the experiment (E2), and we did not adapt these parameters for our 3D simulation. Even so, the 2D and 3D simulations show remarkably good agreement with each other.

5.2 The Contact Angle Model by Shikhmurzaev

In this subsection, we present results for the droplet impact simulation with the reduced interface formation model (C2) combined with the global volume correction for the level-set method. We present two different variants of the model: On the one hand we take Moffatt's solution for the radial velocity (M1) and on the other hand we choose a far field velocity value to incorporate the influence of the flow field on the dynamic contact angle (M2). The parameter Sc is chosen to be 11.5 for (M1) and 5.5 for (M2). We set the values $\rho_G^s = 0.9$ and $\sigma_{sg} = 0$ according to [15].

The results of the laboratory experiments (E1) are always shown in the first row of Figure 8. The droplet shapes computed by (M1) are given in the second row. As with (C1), the first three results are very close to the experimental snapshots, which is to be expected, since inertia dominates capillary effects. In addition, also at the later time steps, the computed droplet shapes agree very well with (E1). At $t = 10$ ms the height and width of the droplet is reproduced very accurately. Further, at $t = 15$ ms, the droplet even forms a little dent before it meets the substrate and compares best with the experiment of all simulation results. A look at the droplet diameter evolution (Fig. 9) confirms that the interface formation model, although it is not

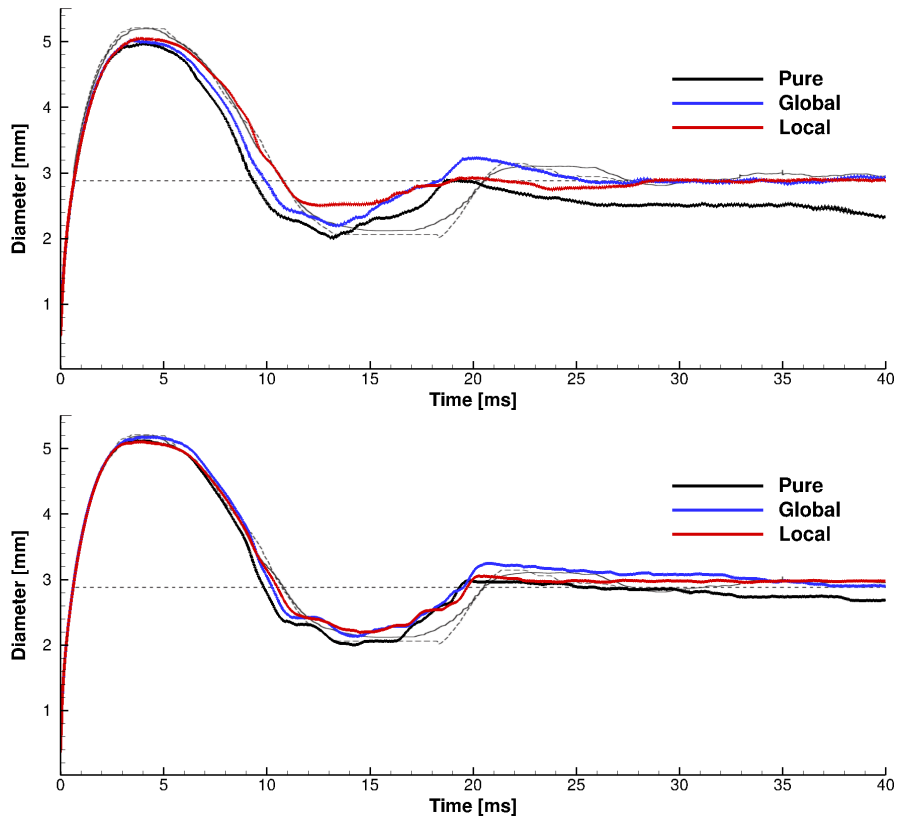


Fig. 7 Comparison of droplet diameter over time with experimental results. Our 3D simulations with the pure level set method (black), global (blue) and local (red) volume correction compared to 2D numerical and experimental results by Yokoi et al. [23]. The theoretical final droplet diameter is given by the straight dashed line. The thin black line corresponds to the 2D numerical results and is very close to that of the experiments given by the thin dashed line. Above, the grid resolution is $121 \times 61 \times 121$ and below it is $241 \times 121 \times 241$.

specifically based on this experiment, produces nearly as good results as Yokoi's model: The maximum and final droplet diameter are captured, and the computed curve is very close to that of the experimental results.

In a next step, we compare the angle-speed curve of the interface formation model (M1) with Yokoi's 2D numerical results and the experiments. We expect that Yokoi's model, since it is fit to this experiment, produces dynamic contact angles which are very close to the ones measured in the experiment. From Shikhmurzaev's model we expect a smooth angle-speed relationship equal to our preliminary computation in Figure 2. This is exactly what we see in Figure 10: The contact angles computed by (C1) are nearly identical to the experimental values, while the ones computed by (C2) develop in a smoother and nearly linear fashion but show a larger

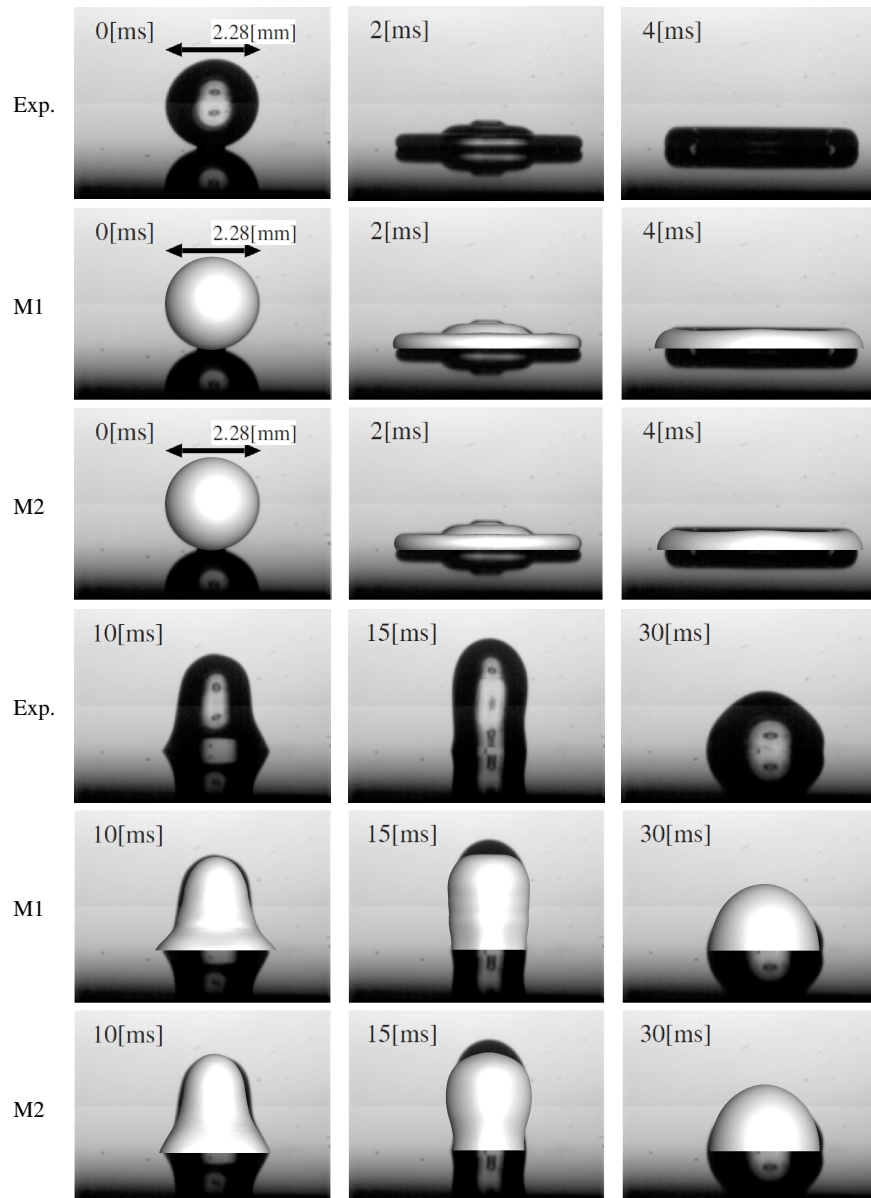


Fig. 8 Droplet impact $t = 0$ to 30 ms. In descending order: experimental results, reduced interface formation model with Moffatt's solution (M1) and $Sc = 11.5$, reduced interface formation model with far field velocity (M2) and $Sc = 5.5$

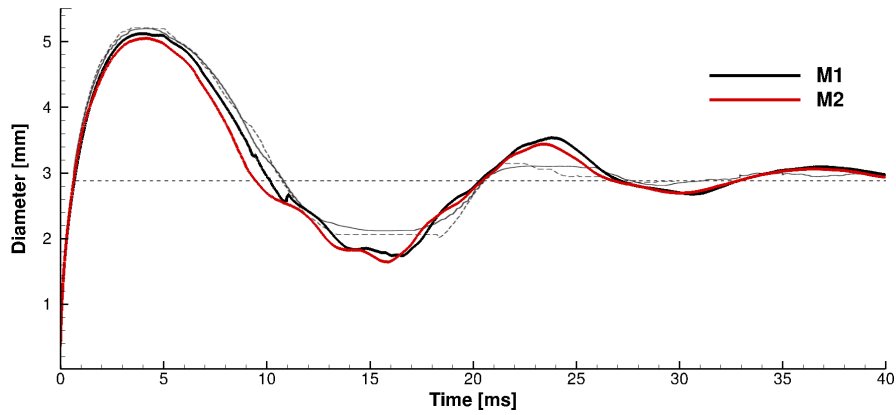


Fig. 9 Comparison of droplet diameter over time with experimental results. Our 3D simulations with M1 (black) and M2 (red) compared to 2D numerical and experimental results by Yokoi et al. [23]. The theoretical final droplet diameter is given by the straight dashed line. The thin black line corresponds to the 2D numerical results and is very close to that of the experiments given by the thin dashed line. Above, the grid resolution is $241 \times 121 \times 241$.

deviation from the experiment. For zero contact line velocity, the model predicts the equilibrium contact angle of 90° . Here, the values measured in the experiment are between 52° and 110° . This is due to the space-time resolution of the experiment, where the contact line velocity is considered to be zero, if the liquid interface does not cross any pixel. Interestingly, however, the smooth speed-angle curve predicted by the interface formation model, lies quite well in between the maximum advancing and minimum receding contact angle of the experiment.

The droplet shapes computed by (M2) are close to the results by (M1) (Fig. 8). Additionally, the droplet diameter varies only little between both models (Fig. 9). Furthermore, in Figure 10, the angle-speed curve shows that both models compute very similar dynamic contact angles in specific regimes of the contact line velocity. For large contact line velocities, (M2) overshoots the maximum dynamic advancing angle determined from the laboratory experiment even more than (M1). However, for small contact line velocities, (M2) tends to be closer to the minimum dynamic receding angle than (M1). The curve for (M2) is scattered, since we use Moffatt's solution, if the contact angle cannot be evaluated directly from the arccos of equation (C2). Here, we observe that for similar contact line velocities both Moffatt's solution and an inserted far field velocity value give similar results with a difference of only a few degrees for the computed contact angle.

All in all, the results by Shikhmurzaev's reduced interface formation model are most promising. Although it is not based on this specific droplet experiment, the computed droplet shapes are very close to those observed in the experiment. Also, the evolving droplet diameter and speed-angle relationship support these very good results.

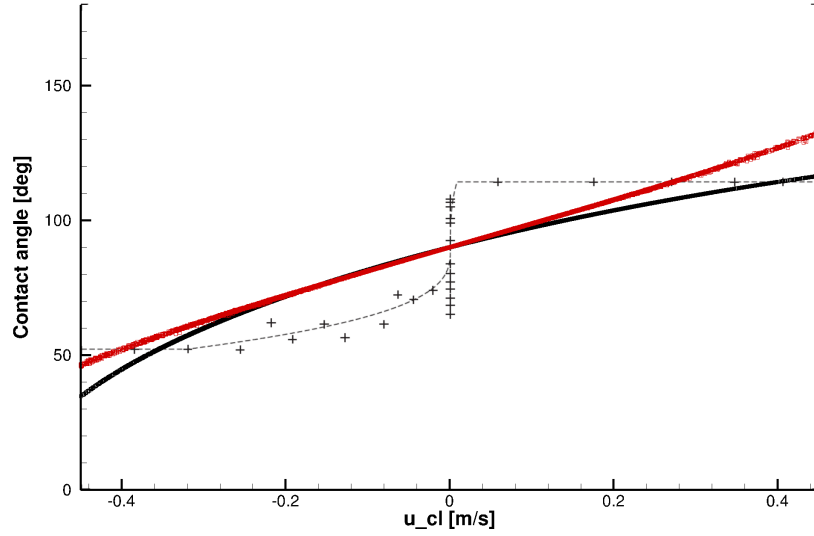


Fig. 10 Angle-speed relationship of a 3D simulation with the reduced interface formation model M1 (black) M2 (red) compared to experiments (+) and 2D simulation with Yokoi's model (dashed), both taken from [23].

Table 2 Details of the mesh used for the mass convergence study (left) and grid convergence of initial mass towards the analytical solution.

Level l	Δx_l	Δy_l	Δz_l	dof_l	$ m_l^0$	ρ_l
1	2.206_{-4}	2.280_{-4}	2.206_{-4}	$31 \times 15 \times 31$	6.511_{-9}	–
2	1.121_{-4}	1.103_{-4}	1.121_{-4}	$61 \times 31 \times 61$	6.281_{-9}	2.020
3	0.565_{-4}	0.561_{-4}	0.565_{-4}	$121 \times 61 \times 121$	6.225_{-9}	1.965
4	0.284_{-4}	0.283_{-4}	0.284_{-4}	$241 \times 121 \times 241$	6.211_{-9}	1.985

Table 3 Volume conservation in % at $t = 30$ ms.

Level l	Pure	Local	Global
1	0	64.4	100.0
2	39.5	91.5	100.0
3	62.8	96.4	100.0
4	78.9	99.3	100.0

5.3 Mass Conservation

In this subsection, we investigate the mass convergence behavior of our numerical schemes for the impact of water on hydrophobic siliane. First, we measure how well the analytical sphere volume can be initially approximated on our computa-

tional grids. Then, we investigate how much volume can be conserved with the pure level-set method and the two volume correction methods at time $t = 30$ ms, which corresponds to the last time-step in Figure 6. Last, we study the convergence of the mass error. The details of the grids used for our convergence study are given in Table 2.

The analytical volume of the sphere, computed from the parameters in Table 1 is $V = \frac{4}{3}\pi r^3 = 6.2059_{-9}$. We evaluate the initial mass of the droplet as

$$m_l^0 = \sum_{\mathbf{x}_i} H(\phi_l^0(\mathbf{x}_i)) \Delta x_l \Delta y_l \Delta z_l \quad (33)$$

on grid levels $l = 1 \dots 4$ as given in Table 2. Then, at time $t = 0$, the discrete error norm and convergence rate are evaluated as

$$e^l = |m^l - V| \text{ and } \rho^{l+1} = \frac{\log \frac{e^l}{e^{l+1}}}{\log 2}, \quad (34)$$

since there holds $2h_l \approx h_{l+1}$ for the discrete mesh width. The convergence results are given in Table 2. We clearly see that initial sphere volume shows second-order convergence towards the analytical value.

In a next step, we quantify the volume loss of our numerical schemes after 30 ms, which corresponds to the last droplet shapes displayed in Figure 6. We expect that the local volume-correction will perform worse than the global volume correction at least on the coarser grids, since the local volume correction only prevents the straying of the level-set function, but does not correct mass errors which occur due to the numerical diffusion introduced when solving the transport equation (10). The global volume correction, on the other hand, employs an absolute stopping criterion of $\varepsilon = 10^{-7}$ in the fixed point iteration and we anticipate to find a very small error in volume for all mesh sizes.

Thus, we measure the volume

$$m_l^t = \sum_{\mathbf{x}_i} H(\phi_l^t(\mathbf{x}_i)) \Delta x_l \Delta y_l \Delta z_l \quad (35)$$

at $t = 30$ ms and compare it to the initial sphere volume at $t = 0$. In Table 3 the percentage of the still remaining volume is given. Mass conservation with the pure level-set method is difficult for this particular case: On the coarsest grid, no mass is left after $t = 30$ ms and on the finest grid, we still loose about 20% of mass. However, both the local and the global volume correction method tend to near 100% mass conservation on the finest grid. As we expected, the global volume correction is able to conserve 100% of mass on all meshes, while the local volume correction performs worse on coarser grids.

Last, we distinguish the effects of the pure level-set method and the local and global volume correction on the overall convergence behavior in space and time at $t = 2$ ms. We compute the discrete error norm and convergence rate by

Table 4 Table of mass convergence for the three level-set methods.

Level	Pure Level-Set		Local Correction		Global Correction	
	e^l_{pure}	ρ^l_{pure}	e^l_{local}	ρ^l_{local}	e^l_{global}	ρ^l_{global}
1	1.587 ₋₁	–	9.572 ₋₂	–	3.453 ₋₈	–
2	7.152 ₋₂	1.150	2.954 ₋₂	1.696	2.769 ₋₈	0.318
3	2.633 ₋₂	1.442	1.114 ₋₂	1.408	4.342 ₋₈	–0.649
4	8.971 ₋₃	1.553	3.897 ₋₃	1.515	6.412 ₋₈	–0.562

$$e^l = \frac{|m_l^t - m_l^0|}{|m_l^0|} \text{ and } \rho^{l+1} = \frac{\log \frac{e^l}{e^{l+1}}}{\log 2}, \quad (36)$$

since there holds $2h_l \approx h_{l+1}$ for the discrete mesh width. Our results are summarized in Table 4, where we see at least first order convergence for the pure level-set method and the local volume correction in space and time. As expected, the discrete error for the global volume correction is constant $< 10^{-7}$ due to the absolute stopping criterion. Therefore, we obtain a convergence rate $\rho^l_{\text{global}} \approx 0$.

6 Conclusion

In this paper we presented the numerical simulation of droplet impact with two different models for the dynamic contact angle in three space dimensions. First, we used Yokoi's model. The resulting droplet shapes were very close to those of the experiments and the previous two-dimensional results. Furthermore, we measured the droplet diameter over time, which confirmed the validity of the model and our numerical method. Here, we saw that both, the global and the local volume correction, are able to conserve the mass of the droplet, while still giving accurate results.

In a next step, we employed the reduced interface formation model by Shikhmurzaev for the droplet impact simulation, combined with the local volume correction. Here, we used Moffatt's solution for the radial velocity on the one hand, and a far field velocity value near the contact line but within the bulk flow on the other hand. The droplet shapes computed with this model were very close to each other and in excellent agreement with the experiment, as also confirmed by the computation of the droplet diameter over time.

Additionally, we compared the contact line speed–contact angle curve of Shikhmurzaev's model with the angle–speed curves of the experiments and Yokoi's model. As was to be expected, Shikhmurzaev's reduced model gives an approximate smoothed angle–speed relationship compared to the practical experiments and Yokoi's results. Thus, a future challenge might be to implement the full interface formation model without any restrictions for the capillary number in three dimensions. But still, the reduced model offers an excellent trade-off between the complex and costly full model and an easily implementable and accurate dynamic contact angle

model, which is not restricted to a specific wetting experiment like Yokoi's model is.

In a last step, we compared the pure level-set method with the two volume correction methods concerning their ability to conserve mass. On the finest grid, both the local and the global volume-correction were able to conserve about 100% of the droplet's mass, while the pure level-set method only retained about 80%. We are currently implementing a coupled level-set and volume-of-fluid method, which should further improve the mass conservation behavior of our flow solver.

Acknowledgements The authors acknowledge the support from the Sonderforschungsbereich 611 "Singular Phenomena and Scaling in Mathematical Models" of the Deutsche Forschungsgemeinschaft DFG. We are grateful to Kensuke Yokoi (Cardiff University) for providing the experimental and numerical results of the droplet impact and the permission to use the corresponding pictures in this article.

References

1. Blake, T. D., Bracke, M., Shikhmurzaev, Y. D.: Experimental evidence of nonlocal hydrodynamic influence on the dynamic contact angle. *Phys. Fluids* **11** (9), 1995–2007 (1999)
2. Brackbill, J. U., Kothe, D. B., Zemach, C.: A continuum method for modeling surface tension. *Journal of Computational Physics* **100**, 335–354 (1992)
3. Croce R., Griebel M., Schweitzer M. A.: A parallel level-set approach for two-phase flow problems with surface tension in three space dimensions. Preprint 157, Sonderforschungsbereich 611, Universität Bonn (2004)
4. Croce R., Griebel M., Schweitzer M. A.: Numerical simulation of bubble and droplet deformation by a level set approach with surface tension in three dimensions. *International Journal for Numerical Methods in Fluids* **62** (9), 963–993 (2010)
5. Decent, S. P.: Hydrodynamic assist and the dynamic contact angle in the coalescence of liquid drops. *IMA J. Appl. Math.* **71** (5), 740–767 (2006)
6. Fang, C., Hidrovo, C., Wang, F., Eaton, J., Goodson, K.: 3-D numerical simulation of contact angle hysteresis for microscale two phase flow. *International Journal of Multiphase Flow* **34**, 690–705 (2008)
7. Goodwin, R., Homsy, G. M.: Viscous flow down a slope in the vicinity of a contact line. *Phys. Fluids A* **3** (4), 215–528 (1991)
8. Hocking, L. M.: A moving fluid interface. Part 2. The removal of the force singularity by a slip flow. *Journal of Fluid Mechanics* **79** (2), 209–229 (1977)
9. Liu, J., Nguyen, N. T., Yap, Y. F.: Numerical studies of sessile droplet shape with moving contact lines. *Micro and Nanosystems*, **3** (1), 56–64 (2011)
10. Moffatt, H. K.: Viscous and resistive eddies near a sharp corner. *Journal of Fluid Mechanics* (18) (1), 1–18 (1964)
11. Monnier, J., Witomski, P.: Analysis of a local hydrodynamic model with Marangoni effect. *Journal of Scientific Computing* **21** (3), 369–403 (2004)
12. van Mourik, S.: Numerical modelling of the dynamic contact angle. Master's thesis, University of Groningen (2002)
13. Mukherjee, A., Kandlikar, S. G.: Numerical study of single bubbles with dynamic contact angle during nucleate pool boiling. *International Journal of Heat and Mass Transfer* **50**, 127–138 (2007)
14. ParaView. <http://www.paraview.org>.
15. Shikhmurzaev, Y. D.: *Capillary Flows with Forming Interfaces*, Chapman & Hall/CRC, 2008

16. Sibley, D. N., Savva, N., Kalliadasis, S.: Slip or not slip? A methodical examination of the interface formation model using two-dimensional droplet spreading on a horizontal planar substrate as a prototype system. *Phys. Fluids* **24**, 082105 (2012),
17. Somalinga, S., Bose, A.: Numerical investigation of boundary conditions for moving contact line problems. *Phys. Fluids* **12** (3), 499, (2000)
18. Spelt, P. D. M.: A level-set approach for simulations of flows with multiple moving contact lines with hysteresis. *Journal of Computational Physics* **207**, 389–404 (2005)
19. Sprittles, J. E., Shikhmurzaev, Y. D.: Finite element simulation of dynamic wetting flows as an interface formation process. *Journal of Computational Physics* **233**, 34–65 (2013)
20. Sussman, M., Fatemi, E.: An efficient, interface-preserving level set redistancing algorithm and its application to interfacial incompressible fluid flow. *SIAM Journal on Scientific Computing* **20** (4), 1165–1191 (1999)
21. Sussman, M.: An adaptive mesh algorithm for free surface flows in general geometries. In: Vande Wouwer, A., Saucez, Ph., Schiesser, W. E. (eds.) *Adaptive Method of Lines*, pp. 207–231. Chapman and Hall/CRC (2001)
22. Tanner, L. H.: The spreading of silicone oil drops on horizontal surfaces. *J. Phys. D: Appl. Phys.* **12** (9) 1473 (1979)
23. Yokoi, K., Vadillo, D., Hinch, J., Hutchings, I.: Numerical studies of the influence of the dynamic contact angle on a droplet impacting on a dry surface. *Phys. Fluids* **21** (7), 072102 (2009)
24. Yun-chao, S., Chun-hai, W., Zhi, N.: Study on wetting model with combined Level Set-VOF method when drop impact onto a dry surface. In: *Electronic and Mechanical Engineering and Information Technology (EMEIT), 2011 International Conference on Electronic & Mechanical Engineering and Information Technology*, pp. 2583–2586 (2011)
25. Zahedi, S., Gustavsson, K., Kreiss, G.: A conservative level set method for contact line dynamics. *Journal of Computational Physics* **228**, 6361–6375 (2009)